



Excess Conductivity of High-Temperature Superconductors Polycrystalline $Y_3Ba_5Cu_8O_{18\pm\delta}$ Doped with TiO_2 Nanoparticles

Siamak Ghahramani¹ · Gholamabbas Shams¹ · Zahra Soltani¹

Received: 25 December 2020 / Accepted: 18 August 2021 / Published online: 1 September 2021
© The Author(s), under exclusive licence to Springer Science+Business Media, LLC, part of Springer Nature 2021

Abstract

Syntheses of the $Y_3Ba_5Cu_8O_{18\pm\delta}$ (noted Y-358) +x wt.% TiO_2 (x = 0.00, 0.10, 0.30, 0.50 and 0.60 wt%) bulk superconducting material are prepared by the standard solid-state reaction process. Then, systematic electrical conductivity fluctuation in normal and superconducting state analyses on the samples is reported. X-ray diffraction (XRD) and scanning electron microscopy (SEM) are used to systematically assess stage formation and microstructures of the samples. XRD with the Rietveld refinement procedure showed that by cumulating the amount of TiO_2 nanoparticle into Y358 substance, the crystal lattice constants altered slightly and the orthorhombicity reduced compared to the pure sample. The impact of TiO_2 adding upon the superconducting characteristics with critical temperatures T_c analysis showed that as the inclusion of TiO_2 nanoparticles content increases the critical temperatures are enhanced for all of the doped samples. Evaluations of excess conductivity fluctuation were conducted by Aslamazov–Larkin (AL) model. Inside the grains, dimensional fluctuation is depending on the Lawrence–Doniach (LD) temperature named T_{LD} . This parameter (T_{LD}) was increased in the mean-field area by rising TiO_2 in Y358 substance compared to the non-added sample. However, analysing the excess conductivity based on the AL concept leads to the determination of thermodynamic fluctuation and some parameters values such as the critical temperature ($T_{c\ zero}$), coherence length $\xi_c(0)$, super-layer length d , critical magnetic fields $B_{c1}(0)$, $B_{c2}(0)$ and critical current density $J_c(0)$. These parameters which are significant by the TiO_2 nanoscale doping show that the theory outlined in the chapter “Excess conductivity model” is sufficient to describe our results.

✉ Gholamabbas Shams
shams@iaushiraz.ac.ir; shams_physics@yahoo.com

Siamak Ghahramani
siamakghahramani@gmail.com

Zahra Soltani
zsoltany@yahoo.com

¹ Department of Physics, Shiraz Branch, Islamic Azad University, Shiraz, Iran

Keywords Excess conductivity · Critical parameters · Y-358 · TiO₂ nanoparticle

1 Introduction

Soon after the first observation of excess conductivity exceeding critical temperature (T_c), in high-temperature superconductors (HTSCs) in 1986 [1], scientists pursued some theoretical and experimental investigation on this effect [2–5]. They recommended in their determinative research that this phenomenon associated with critical fluctuations may be due to thermodynamic fluctuations. This effect had been reported also for conventional “low-temperature” metallic superconductors previously [6]. The excess conductivity which is strongly dependent on the system dimensionality [2] has a substantial prominence as a property of the superconductor characteristics not only related to low-temperature superconductors (LTSCs) [7] but also HTSCs. Superconducting order parameter fluctuations (SCOPF) are affected significantly by three distinctive factors named high critical temperature, anisotropy [8, 9] and actual small coherence length [10]. These parameters are exclusive characteristics related to HTSCs. So as to elucidate these characteristics and consequently explain the framework of the YBCO superconductors and parallel to the development of nanotechnology, scientists have been comprehensively considered HTSCs by various nano-dope entities such as Mg, ZnO, MnO and CoFe₂O₄ [11–13]. Couple of nanoscale inclusions alike NiO and CeO₂ improve some properties of YBCO superconductors [14, 15].

Specific impurity similar to titanium oxide (TiO₂) compound or titania is an important semiconductor which has shown to be a superlative nominee for support of hard resources as superconducting ceramics. The structural crystallography of titanium dioxide is divided into three forms: brookite, rutile and anatase. Among these phases, anatase is the most attractive one because of its broader band gap and superior photocatalytic action regarding research applications in different fields [16–19]. The influence of TiO₂ nanoscale insertion on the specific HTSCs like magnesium and bismuth-based superconducting compounds has been formerly considered [20, 21]. According to the literatures for YBCO compounds TiO₂ semiconducting nanoparticles were inserted to Y123 samples. The titanium dioxide nano-sized particles were not occupied the yttrium position in the Y123 system although had been detected in X-ray diffraction procedures. TiO₂ caused an enhancement of critical current density in Y123 composites which implies the capability of the flux pinning effect [22]. In another research, the Ti replaces the Cu in the Cu positions [23]. Comparing the valence states parameters of Ti⁴⁺ and Cu²⁺ shows that this parameter related to Cu is lower than Ti and replacement of titanium for copper might cause the reduction of the moveable carrier quantity because of hole padding by titanium.

However, nanoparticles addition in superconducting compounds is an essential method to demonstrate a simple method without any destruction and effective instrument for refining the physical and characteristics of the added composites. Nanoparticle addition might also cause unforeseen variations in the behaviour of the superconductors [24]. For determination whether the characteristics of superconductors are enhanced or destroyed, type, size and amount of inclusion are the main factors.

A large range of nanostructures were manufactured during nanotechnology developments and their influence on the HTSCs was examined. When a suitable quantity of nanoscale substances is inserted into the yttrium-based superconducting matrix, the flux pinning and the transport properties might conceivably be improved. For example, rising in critical current density occurred while carbon with nanotubes feature was inserted to Y123 superconductor similar to pinning centres [25]. The results of another experiment propose that at a temperature about boiling liquid nitrogen the additional TiO_2 nanoparticles might generate great pinning effectiveness [22]. Stability of nanoparticles at raised temperatures and nanoscale of doping substances corresponding to the coherence length of the HTSCs are two main necessities associated with the flux pinning efficiency related to the high-temperature superconductors [26]. In the current decade, some theoretical and experimental research has been done on fundamental and mechanical properties of $Y_3Ba_5Cu_8O_{18\pm\delta}$ materials [27–29]. Applying titanium dioxide nanoparticles in Y358 compound might demonstrate to be helpful as enlightening the implementations of superconducting properties. However, there are hardly any detailed reports on the properties of YBCO doped by anatase TiO_2 nanoparticles. Eager for investigation regarding this subject has triggered great interest in Y358 material in the field of superconductivity. Therefore, for a precise endorsement of the effect of TiO_2 addition further research would be obligatory from a pure superconductor technology point of view.

In this work for the first time, we have examined the effectiveness of TiO_2 nanoparticles inclusion in the high-temperature bulk superconductor $Y_3Ba_5Cu_8O_{18\pm\delta}$ specimens. These materials are fabricated via conventional solid-state feedback route. Measurements have been performed on the superconducting properties of these polycrystalline compounds with different weights of nanoscale titanium dioxide substances ($x = 0.00 - 0.60$ wt. %) with 20 nm size. Analysing the behaviour of thermal fluctuations conductivity over T_c and also determination of some variations in pristine and added composites have been made. This process achieved in the Lawrence–Doniach (LD) system and framework of Aslamazov–Larkin (AL) concept. We obtained some superconducting parameters such as boundary temperature from 3D to 2D (T_{LD}), the coherence length alongside the c-axis at zero temperature $\xi_c(0)$, real super-layer length of the two-dimensionality classification d and interlayer coupling J . We calculated furthermore the anisotropy γ related to schemes of layered superconductor and the following critical parameters at (0) Kelvin: thermodynamic critical field, the lower and upper critical magnetic fields and eventually the critical current density which are symbolised by $B_c(0)$, $B_{c1}(0)$, $B_{c2}(0)$ and $J_c(0)$, respectively.

2 Experimental Details

Titanium oxide nanoparticles (TiO_2 , anatase, 99+%, 20 nm) were prepared from US Research Nanomaterials, Inc located in Houston, TX, USA. Purity of the titanium oxide nanoparticles is higher than 99% with bulk density: 0.46g/ml, the average particle size: 20 nm. Pure $Y_3Ba_5Cu_8O_{18\pm\delta}$ and added with nanoscale TiO_2 specimens were prepared by the standard solid-state feedback process. Consistent with the substance procedure the fractions of Y:Ba:Cu = 3:5:8, polycrystalline Y358

was manufactured with elevated cleanliness (99.9%) powders of Y_2O_3 , Ba_2CO_3 and CuO which are made in Germany (Merck company). The mixtures were pressed into pellets and then calcination process followed during twelve hours at $900^\circ C$ and repeated two times. Throughout the last procedure phase, TiO_2 nanoparticles were added to the mixtures of Y-358. Then, the blends were mixed and ground suitably in an agate mortar. The added quantity of TiO_2 diverse from $x = 0.00$ to 0.60 wt% for the entire amount of the specimen. The mixtures were pushed within containers at two hundreds bars in the round discs shape with dimensions of $30mm \times 4mm$. After inserting the samples in a quartz pipe, the sintering procedure occurred at $950^\circ C$ and followed for two days in vicinity of oxygen atmosphere and next declined to $25^\circ C$ with $4^\circ C/min$ rate.

Samples preparation followed by specification of sintered compounds powder using X-ray diffraction (XRD) technique to identify phase and configuration of pure and added with TiO_2 nanoscale upon Y358 specimens in the angle variety of $2\theta = 10^\circ \sim 80^\circ$. Materials Analysis Using Diffraction (MAUD) software beside the Rietveld refinements was used to determine the lattice factors a , b and c whereas the oxygen quantity is assessed. Microstructures of the samples were categorised by scanning electron microscopy (SEM) technique and finally resistivity experiments performed to calculate excess conductivity. Resistivity measurements were undertaken with four-point probe technique. To achieve these experiments the pellets are carefully cut into $\sim 20 \times 5.5 \times 2.2$ mm³ sizes to make almost identical bar shape samples. DIL package sample holder provided by SPECTRUM Semiconductor Material INC, was used to mount the samples. The samples were attached to the sample holder by zinc oxide paste. Colloidal silver was used to attach current and voltage wires onto the sample surface at the position of evaporated silver pads. Electrical contact resistance values are estimated to be less than 0.1Ω . In order not to affect the superconducting transition properties, a low current 100 mA ($I \ll I_C$: the critical current) was carried through the current wires. Measurements were accomplished with an accuracy of 0.1 K while sweeping up (and down) at the rate of $1^\circ C/min$. Two resistivity experiments runs were performed for each sample to make a trustworthy quantitative analysis of the outcomes, one for cooling down sweep, the other for warming up sweep. These subjects are elucidated with further details in another research paper [30].

Subdivision method [31] is performed and monitored by producing a dual picture to display particles more clearly in SEM images. The pixels intensity below the minimum threshold value displayed in blue (background contribution) and the pixels intensity above the maximum threshold value depicted in green colour for better exhibition of particles.

3 Excess Conductivity Method

Thermodynamic fluctuations produces the excess conductivity over critical temperature according to the Aslamazov–Larkin concept which delivers the following equation: [32].

$$\Delta\sigma = A/\varepsilon^\nu \quad (1)$$

Here, A named Aslamazov–Larkin constant and ε denotes the reduction temperature transition from non-superconducting to superconducting state with the next equation:

$$\varepsilon = (T - T_C^P)/T_C^P \quad (2)$$

where T_C^P denotes the temperature of the highest value related to derivative of resistivity versus temperature curve. ν so-called the critical exponent dependent on the superconducting scheme's dimensionality. Based on the Aslamazov–Larkin (AL) model [32] and related to the mean-field section, the instability stimulated excess conductivity $\Delta\sigma$ is usually computed by the following formula [33]:

$$\Delta\sigma = \left(\frac{1}{\rho_m} - \frac{1}{\rho_n} \right) = \sigma_m(T) - \sigma_n(T) \quad (3)$$

where ρ_m and ρ_n are the measured and normal resistivities, respectively. $\sigma_m(T)$ represents the measured conductivity and $\sigma_n(T)$ displays the normal conductivity which is obtained by extrapolation of linear resistivity $\rho(T) = 1/\sigma(T)$ over $2T_C$. Note that the figure of the non-superconducting resistivity (ρ_n) versus T is approximately linear as follows:

$$\rho_n(T) = \rho_0 + \beta T \quad (4)$$

whereas ρ_0 and β are residual and slope of the line, respectively. Extrapolating to this line leads to achieve σ_n successively. The following equation shows the relationship between dimensionality D and critical exponent ν .

$$D = 4 - 2\nu \quad (5)$$

In the critical fluctuation region closer to transition temperature T_c wherever fast formation occurs, termination of Cooper pairs appears. Between the granules of superconductors, Josephson coupler appears and rise their interaction in two-dimensionality state if the magnetic field does not exist. The responsibility of CuO₂ planes in high-temperature superconductors are not only dimensionality but also anisotropy. Relationship between the critical exponent of excess conductivity (ν_{cr}) and the critical exponent aimed at the coherence length (Γ) is displayed by Drude formula as follows [11, 34–37]:

$$\Gamma = \frac{\nu_{cr}}{2 - D + \eta + Z} \quad (6)$$

here D named the dimensionality of the fluctuations, η called the exponent of the order parameter correlation function and Z termed the dynamical exponent. The exponent related to the critical exponent for two- and three-dimensionality systems are $\nu = 1$ and $\nu = 0.5$ correspondingly [38]. The exponent quantities are determined from the slopes of fitting line to the graphs of $\ln(\Delta\sigma)$ versus $\ln(\varepsilon)$ for pure and added Y358 with TiO₂ nanoparticle samples. Three discrete fluctuation arrangements

might be illustrated in each graph so-called Gaussian (mean field), critical and short-wave fluctuation zones.

The standards temperature reliant factor (A) are $A_{3D} = \frac{e^2}{32\hbar\xi_c(0)}$, $A_{2D} = \frac{e^2}{16\hbar d}$ and $A_{1D} = \frac{e^2\xi_c(0)}{32\hbar s}$ which symbolised for three-, two- and one-dimensionality systems correspondingly. “ $\xi_c(0)$ ” itemised the coherence length at (0) Kelvin, “ d ” named the active distance of CuO2 planes and “ s ” labelled the wire cross section zone of the one-dimensionality scheme, individually. According to the Ginzburg–Landau model, these relationships are effective just for $1.01T_c$ to $1.1T_c$ (mean field) area. For high superconducting compounds the LD and AL models complement each other and explain how conduction appears essentially in two-dimensionality CuO2 layered where the layered are paired by Josephson tunnelling. The excess conductivity analogous to the planes in the Lawrence and Doniach report specifies as:

$$\Delta\sigma(T)_{LD} = \frac{e^2}{16\hbar\epsilon d \left[1 + \left(\frac{2\xi_c(0)}{d} \right)^2 \epsilon^{-1} \right]^{1/2}} \quad (7)$$

From the above equation at a temperature close to T_c , $2\xi_c(0)/d \gg 1$ and $\Delta\sigma(T)$ deviates like $\epsilon^{-1/2}$ which relates to three-dimensionality behaviour. But at $T \gg T_c$, $2\xi_c(0)/d \ll 1$ and $\Delta\sigma(T)$ deviates by way of ϵ^{-1} which agrees with two-dimensionality behaviour. Regarding superconducting composites and at the changeover temperature, T_{3D-2D} , the coherence length alongside c-axis, $\xi_c(0)$ would be attained by the LD propose [39]:

$$T_{2D-3D} = T_c + T_c \left(\frac{2\xi_c(0)}{d} \right)^2 \quad (8)$$

With this theory, the idea of interlayer pairing, J established by Josephson coupling as an outcome of $\xi_c(0)$ collaboration with the layered superconductors can be specified as follows:

$$J = \left(\frac{2\xi_c(0)}{d} \right)^2 \quad (9)$$

Each term defined lately is involved in the suitable generality of the AL theory related to the excess conductivity. This is being effectively performed to clarify the development of paraconductivity because of the attendance of thermal instabilities of Cooper pairs beyond T_c , in the high-temperature superconductors (HTSCs). These composites are always recognised with the characteristics such as strong anisotropy (γ), high T_c and small coherence length ($\xi_c(0)$), when applied electric field is small or zero and magnetic field is not applied. AL expression of paraconductivity can be written as following formula [40]:

$$\Delta\sigma = \frac{e^2}{16\hbar s} f(\epsilon) \quad (10)$$

where $f(\varepsilon)$ named universal function which can be shown as one of the subsequent features, dependent on the shortened temperature, ε :

- 1) In the case of $\varepsilon \ll 1$ the Gauss–Ginzburg–Landau (GGL) of two-dimensionality paraconductivity is taken into account and explained by AL concept:

$$f(\varepsilon) = \varepsilon^{-1} \quad (11)$$

- 2) When $\varepsilon \geq 0.1$, another condition occurs and the short wavelength fluctuations (SWF) resemble while their typical wave distance turn out to be comparable to the coherence length, $\xi(0)$. Inside SWF area in the limit of non-cutoff system we can write:

$$f(\varepsilon) = \varepsilon^{-3} \quad (12)$$

The anisotropy γ related to high-temperature superconductors is defined by [41]:

$$\gamma = \frac{\xi_{ab}(0)}{\xi_c(0)} \quad (13)$$

where $\xi_{ab}(0)$ is the coherence length in ab plain with the amount of ten to twenty angstroms aimed at YBCO HTSCs [39]. The Ginzburg number can be obtained experimentally as follows:

$$N_G = \left| \frac{T_G - T_C}{T_C} \right| \approx 10^{-3} \left(\frac{\hbar}{B_c(0)\xi_c^2(0)\gamma e} \right) \quad (14)$$

where T_G , T_C , $\hbar = \frac{h}{2\pi}$ and $B_c(0)$ are entitled the temperature related to termination of three-dimensionality system, the critical temperature, the Plank's constant/ 2π and the thermodynamic critical field, respectively. Relationship between the thermodynamic critical field $B_c(0)$, the flux quanta φ_0 and the penetration depth $\lambda(0)$ is formulated by:

$$B_c(0) = \frac{\varphi_0}{2\sqrt{2}\pi\lambda(0)\xi_c(0)} \quad (15)$$

Substituting the value of $B_c(0)$ into the Ginzburg–Landau formula some critical parameters such as the lower, the upper critical magnetic fields, $B_{c1}(0)$, $B_{c2}(0)$ and critical current density $J_c(0)$ are computed using the next equations:

$$B_{c1} = \frac{B_c \ln \kappa}{\sqrt{2}k} \quad (16)$$

$$B_{c2} = \kappa B_c \sqrt{2} \quad (17)$$

$$J_c = \frac{4\kappa B_{c1}}{3 \ln \kappa \sqrt{3}\lambda} \quad (18)$$

here κ is the fraction of the penetration depth to the coherence length and is defined the Ginzburg–Landau parameter.

4 Results and Discussion

The measured XRD spectra of TiO₂ nanopowder, Y-358 pure and doped with diverse quantities of TiO₂ nanoparticles varying 0.00 to 0.60 wt.% are shown in Fig. 1. The XRD spectra are measured from 10 to 80°. According to TiO₂ nanoparticles 9 peaks at 2θ values of 25.27°, 37.85°, 48.02°, 53.93°, 55.14°, 62.66°, 68.79°, 70.34° and 75.12° can be observed which are associated with (101), (004), (200), (105), (211), (204), (116), (200) and (215) (Miller's Indexes), respectively. A matching of the observed and standard (hkl) planes confirmed that the TiO₂ nanoparticles with lattice parameters of $a = 3.78520 \text{ \AA}$, $b = 3.78520 \text{ \AA}$ and $c = 9.51390 \text{ \AA}$ having a tetragonal structure, with the Average Particle Size APS(D50) 20 nm. The X-ray diffraction analysis revealed that space group regularity and construction phase of the samples are Pmm2 and orthorhombic, respectively. In these XRD graphs, 18 diffraction peaks are apparent at $2\theta = 15.33^\circ$ to 77.88° consistent with the planes of orthorhombic $Y_3Ba_5Cu_8O_{18\pm\delta}$. The main peaks are in good agreement with Y-358

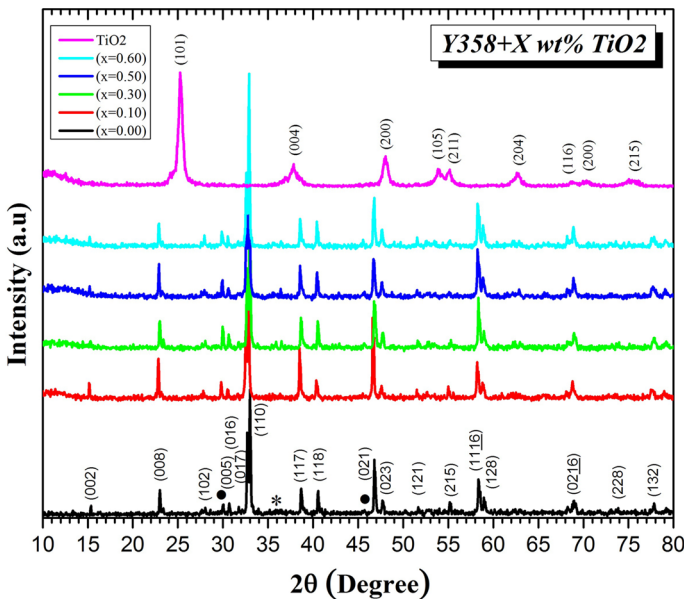


Fig. 1 XRD patterns of the TiO₂ nanoparticles powder accompany with the samples of pure Y-358 and doped TiO₂ nanoscales. Symbols (•) and (*) illustrate secondary phases related to Y-211 and other impurity, respectively (color figure online)

[28, 29]. Some of the peaks grow by increasing the TiO₂ nanoparticles and demonstrating the improvement of the crystallisation granules. This influence is evident at 32.63° mainly related to $x = 0.60$ wt% which is confirmed by another literature [42]. Secondary phases consistent with the Y-211 and other impurity are also observed in the XRD pattern of the samples by extra peaks between 29° and 46°.

The average crystal sizes of the pure and doped with different amounts of TiO₂ nanoparticles are calculated with the Scherrer's equation [43] according to the following formula:

$$P = \frac{C\lambda_{Cu}}{B \cos \theta} \quad (19)$$

where P is the mean size of the ordered (crystallite) domains, which may be smaller or equal to the grain size; C is a dimensionless shape factor equal to (~ 0.89), λ_{Cu} is the wavelength of XRD ($\lambda_{Cu} = 1.5418\text{\AA}$), B is the full peak width, corrected for instrument broadening at half the maximum (FWHM) of the peak in radian, and θ is the Bragg angle of the diffraction peaks. Five peaks with the most height at 2θ values of 23, 32.82163, 38.70253, 40.44173 and 46.84701 were chosen to obtain crystallite size. These peaks and their traces for obtaining FWHM are depicted in Fig. 2. The average crystallite size was found to be 35.47, 29.76, 32.55, 41.47 and 42.11 nm, for $x = 0.00, 0.10, 0.30, 0.50$ and 0.60 , respectively. The crystallite size of samples was decreased up to $x = 0.30$ wt.% and then increased upon addition of TiO₂.

According to the X-ray diffraction patterns there are no significant modifications with the addition of TiO₂, except for very small peaks at $2\theta = 48.02^\circ$. It is

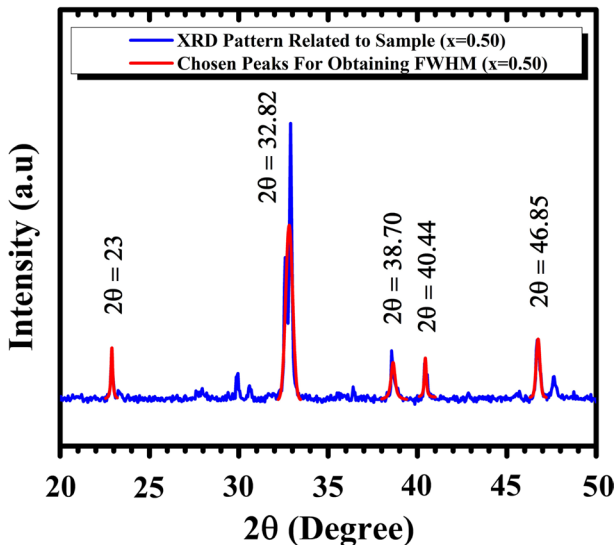


Fig. 2 XRD pattern of the Y-358 + 0.50 wt% TiO₂ nanoparticles sample and chosen peaks with the most height at 2θ values of 23°, 32.82163°, 38.70253°, 40.44173° and 46.84701° for obtaining FWHM and consequently crystallite size of the samples (color figure online)

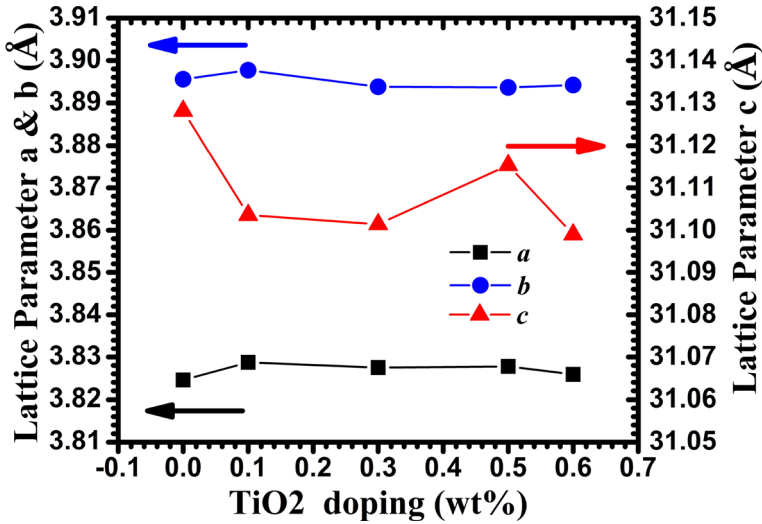


Fig. 3 Variant of lattice constants a , b and c aimed at Y358 specimens doped by different quantities of TiO₂ nanoparticles (color figure online)

Table 1 Structural lattice constants, volume of cell, average crystallite size, calculated density, orthorhombicity and oxygen quantity of Y358 compounds by different additions of TiO₂ nanoparticles

Parameters	x=0.00	x=0.10	x=0.30	x=0.50	x=0.60
$a(\text{Å})$	3.82456	3.82869	3.82747	3.82775	3.82587
$b(\text{Å})$	3.89558	3.89769	3.8938	3.89364	3.89422
$c(\text{Å})$	31.1281	31.10357	31.1014	31.11533	31.09899
Volume of cell abc (Å ³)	463.77	464.16	463.52	463.74	463.34
Average crystallite size (nm)	35.47	29.76	32.55	41.47	42.11
Calculated density (gr/cm ³)	4.55	4.52	4.40	4.32	4.48
Orthorhombicity $Y = (a - b)/(a + b)$	0.0092	0.00893	0.00859	0.00853	0.00885
Oxygen content	17.687	17.620	17.629	17.643	17.641

hard to say these peaks can be associated with TiO₂ addition, because they may be overlapped with the base peaks of Y-358 in x-ray diffraction patterns. However, our results denote that a slight quantity of TiO₂ inclusion mixed with the specimens has no obvious effect on the ultimate outcome in X-ray determination. Obviously, there has not been detected any peak related to the Ti element in XRD configurations.

The lattice constants a , b and c associated with pure and TiO₂ nanoparticles doping samples are shown in Fig. 3 and tabulated also in Table 1. The values of a and b related to the pure compound are 3.82456 Å and 3.89558 Å correspondingly which are in agreement with the data reported by some literatures [27, 44]. The value of lattice parameter c for the pure sample is 31.1281 Å and corresponds to the other [45]. The c lattice constant belongs to Y358 is nearby three times of Y123 [27, 46], whereas the lattice constants a and b of these YBCO family compounds are very

close to each other [27]. Our results show that by inclusion of TiO_2 into Y-358 compound, the lattice constants a and b remain almost constant but the c cell parameters decrease in all cases compared to the pure sample. However, the reduction in c quantity parameters can be accountable for an enhanced interlayer exchange and therefore might cause better characteristics of superconductors [47]. The variation of c parameter and also size of the crystals is anticipated because of the straining result, such as, the tiny scale of the non-uniform flexible twists which has been imposed to the Y358 crystal matrix by titanium insertion. Since the radius of Ti ion is 0.605 \AA and almost 20% lower than Cu ion (0.73 \AA), it might be completely replaced aimed at the copper location [23].

Insertion of some elements such as Co and Fe into the YBCO samples acts differently depending on the doping level. They predominantly localise on the Cu(I) sequence location when the doped level is low. For higher doping levels they locate at the Cu(II) [48, 49]. Nevertheless, by small amount of TiO_2 nanoparticles doping (up to $x = 0.60 \text{ wt\%}$), unimportant variations in the lattice constants occurred. This might be summarised that Ti was not substituted for Y, and in its place most probably contributed as a secondary phase in the system. This argument shows further evidence that the replacement of Ti in the sample does not occur. And there were no significant changes in the lattice constants a , b and c by insertion of TiO_2 nanoparticles into the Y-358 compound.

Computed volume cell achieved by abc relationship and calculated density related to Y-358 composites (varying $x = 0.0 \text{ wt\%}$ to $x = 0.6 \text{ wt\%}$) are illustrated in Fig. 4 and recorded also in Table 1. The volume of cell was found to be 463.77, 464.16, 463.52, 463.74 and 463.34 (\AA^3), for $x = 0.00, 0.10, 0.30, 0.50$ and 0.60 , respectively. The most discrepancy for calculated density is 5% between pure and 0.50% wt. doping samples.

Fig. 5 demonstrates orthorhombicity related to the Y358 structure which was estimated by the lattice constant differences $Y = \frac{a-b}{a+b}$ and is charted also in Table 1

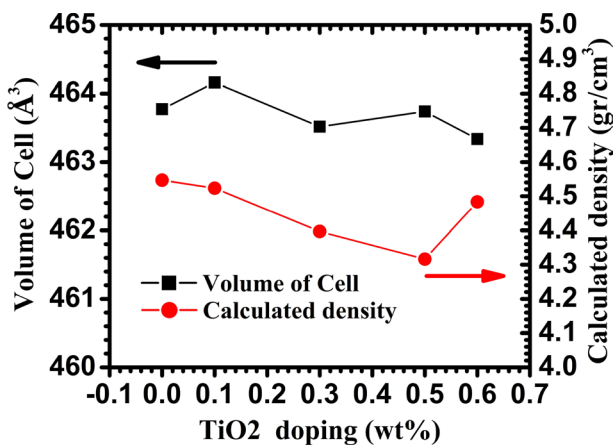


Fig. 4 Disparity of volume cell and calculated density associated with Y358 specimens versus numerous quantities of TiO_2 nanoparticles (color figure online)

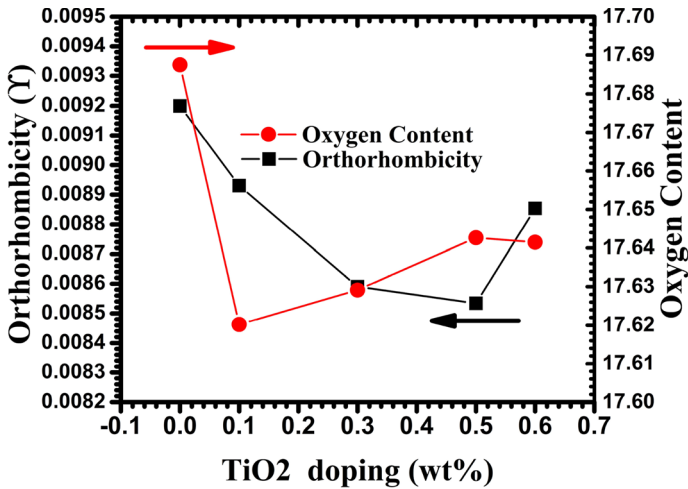


Fig. 5 Variant of orthorhombicity Y and oxygen content aimed at Y358 composites doped by diverse quantities of TiO₂ nanoparticles (color figure online)

[50] for all samples (altering $x = 0.0$ wt % to $x = 0.6$ wt %). The highest orthorhombicity is equal to 9.2×10^{-3} in non-added and lowest is 8.53×10^{-3} in 0.50 wt.% titanium dioxide doped compounds. This quantity is in good agreement with other literatures [23, 51, 52]. Such a great amount of orthorhombicity indicates a high level of oxygen value. The oxygen content for Y358 is also estimated by oxygen determination from cell dimensions similar to Y123 superconductors [53]. The oxygen content obeys the following relationship $O.C = -18.32797 + 4.42504 \times \frac{c}{a}$, where c and a are lattice parameters. The $O.C$ obtained values are 17.687, 17.620, 17.629, 17.643 and 17.641 on behalf of non-added and doped nanoparticles titania mixtures associated with the $x = 0.0$, $x = 0.10$, $x = 0.30$, $x = 0.50$ and $x = 0.6$, respectively. These data related to $Y_3Ba_5Cu_8O_{18 \pm \delta} + x$ wt.% TiO₂ are tabulated in Table 1. According to this table and Fig. 5, reduction of oxygen content occurred when the value of nanoparticles titania increased. Addition of TiO₂ nanoparticles dopant into Y-358 compounds affects both oxygen content and orthorhombicity in such a way that their graphs obey the same tendency. Undeniably, by decreasing the oxygen content the orthorhombicity can be decreased consequently [54]. Recently, some researchers presented that titanium replaces favourably the Cu(2) location in CuO₂ planes. And the orthorhombic arrangement together with the order of oxygen in the CuO sequences stays unaffected even for greater titanium amounts [26], though superconducting state in Y358 is correlated not only to the oxygen content but also to the arrangement of the “O” vacates and “O” particles in the Cu–O plane.

Electrical resistivity versus temperature associated with pure and TiO₂ nanoscale added upon Y358 polycrystalline compounds are illustrated in Fig. 6. This resistivity graph includes two different sections. The primary section is categorised by a metallic behaviour named normal state (beyond $2T_c$). The normal section is formulated by the linear equation $\rho_n(T) = \rho_0 + \beta T$. Here, β is slope constant and ρ_0 is the remaining resistivity. β represents the basic electronic correlation and ρ_0 shows the sample

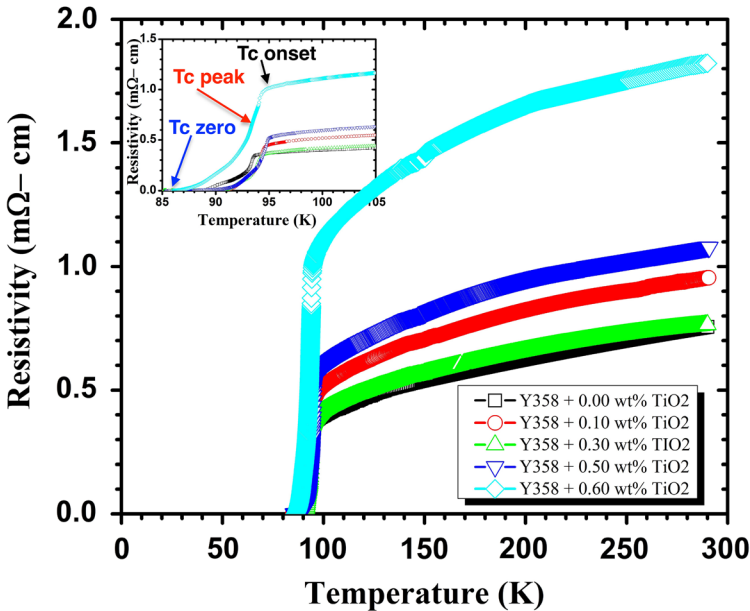


Fig. 6 The plots of ρ against T on behalf of the Y358 specimens including diverse amounts of nano-sized TiO₂. Inset: resistivity plot for exhibiting precise $T_{c\ zero}$, $T_{c\ onset}$ and T_c^P (color figure online)

imperfection solidity. Linear fitting of ρ within the temperature range between $2T_c$ and 290 K by extrapolating to 0 K is used to obtain the values of parameters ρ_0 and β . This is equal to the resistivity slope ($d\rho/dT$) and consequently, end up with determination of $\rho_n(T)$. The second regime belongs to the region lower than critical temperature, where $\rho(T)$ is deviating from linearity. Here, $\rho(T)$ categorised by the influence of Cooper pairs instability to the conductivity below critical temperature. This procedure appears predominantly because of the rising amount of Cooper pair creation during the falling of temperature. Hence, the instability conductivity in this area obeys Aslamazov–Larkin archetype to yield the dimensional exponent suitably. [23].

The initial drop of resistivity in the superconducting transition which was labelled as $T_{c\ onset}$ is shown in Fig. 6. The data regarding these $T_{c\ onset}$ on behalf of compounds added TiO₂ nanoscale $x=0.00$, $x=0.10$, $x=0.30$, $x=0.50$ and $x=0.60$ wt% are 94.37, 95.95, 95.40, 96 and 94.91 K, respectively. These values increase for all doped sample compared to the non-added one. The data are more pronounced for the highest $T_{c\ onset}$ of Y358 which is recorded 94 K previously [55]. For pure Y358, other literature recorded 93 K or higher value 99.98 K depending on preparation of the sample whether melt-texture or solid-state reaction method, respectively [29]. The $T_{c\ onset}$, which is associated with intragranular shielding [56], is depicted in Table 2 in detail. However, the $T_{c\ onset}$ and $T_{c\ zero}$ which are named onset transition temperature and zero-resistance temperature, are the temperatures where the resistivity begins to decline sharply and the resistivity drops to zero, respectively [57]. It is clear that for all of the samples in this study $T_{c\ onset} > T_c^{Peak} > T_{c\ zero}$ which is shown typically

Table 2 Temperature parameters $T_{c\text{ onset}}$, $T_{c\text{ zero}}$, T_C^P and ΔT_c accompany with resistivity factors $\rho_0(0K)$, $\rho_n(290K)$ and β versus TiO_2 nanoscales doped with Y-358 compounds

Parameters	x=0.00	x=0.10	x=0.30	x=0.50	x=0.60
$T_{c\text{ onset}}(K)$	94.37	95.95	95.40	96.01	94.91
$T_{c\text{ zero}}(K)$	88.63	85.18	87.44	85.35	85.99
$T_C^P(K) \Rightarrow d\rho/dT$	93.41	94.27	93.84	94.74	94.07
$T_C^P(K) \Rightarrow \Delta\sigma vs T^{-0.5}$	93.35	94.25	93.85	94.73	94.07
$\Delta T_c(K)$	0.41	0.92	0.94	0.64	0.38
$\rho_0(0K)(m\Omega cm)$	0.43	0.61	0.47	0.72	1.41
$\rho_n(290K)(m\Omega cm)$	0.74	0.95	0.76	1.08	1.82
$\beta = \frac{d\rho}{dt}(\mu\Omega cm)/K$	1.05	1.20	1.00	1.26	1.43

in the inset of Fig. 6 for Y358+0.60 wt.% TiO_2 sample. According to Fig. 6 and its inset, not only the electrical resistivity but also critical temperatures increase for all of the samples compared with the pure one. The outcomes showed that the entire of specimens can be transformed to superconducting state below 85.18 Kelvin. Data related to $\rho_0(0K)$ and $\rho_n(290K)$ associated with Y358+x wt.% TiO_2 impurities are also tabulated in Table 2. In this table, superconducting changeover width, (ΔT_c), which is assessed by the $d\rho/dT$ plots on full width at half maximum (FWHM), is tabulated. For pure Y358 sample (ΔT_c) is around 0.41 K and less than 1 K for samples with TiO_2 addition, implying a good quality of samples. The highest and lowest value of (ΔT_c) is 0.94 and 0.38 K for x=0.30 and x=0.60 wt% correspondingly. The average value of (ΔT_c) increased upon the addition of TiO_2 compared to the non-added sample. This may be certified from differences and characters of granule samples. Based on fluctuation conductivity, characters of grains have important impacts on the characteristics of critical and mean-field regions [12, 28, 58]. Compared to the pristine sample, adding TiO_2 nanoparticles into Y-358 compound cause increasing the normal state resistivity in all (doped) samples. Increase in resistivity can be explained by procedure which is responsible for distribution of electron scattering. This is not only associated with the small but also with the big incline grain borders related to the dissimilar structural arrangements. In the non-superconducting state, the entire resistivity can be correlated to porosity and granule border expansion. The linear resistivity around a longer temperature interval supports this idea that the formulation and manufacture of the all composites including pure and added TiO_2 nanoparticles into Y358 mixtures are completed properly.

As it mentioned before the most common technique which is differentiating of resistivity related to temperature ($d\rho/dT$) was performed to determine the T_c . The temperature associated with the peak of this curvature identifies the critical temperature of Y358 superconductors T_C^P and is shown in Fig. 7 and also listed in Table 2. Another criterion for the definition of T_C^P is based on 3D AL framework [59]. According to this outline T_C^P can be obtained by $\Delta\sigma(T)$ curves. Nearby the critical temperature T_c while the temperature comes close enough to T_C^P , the $\Delta\sigma$ will diverge as $(T - T_C^P)^{-0.5}$, follow-on $\Delta\sigma(T) \propto (T - T_C^P)^{-0.5}$. Therefore, the T_C^P can be obtained by a linear fitting to the experimental data associated with the $\Delta\sigma$ versus $T^{-0.5}$ curve. The linear fitting which is related to 3D AL fluctuation section can be extrapolated

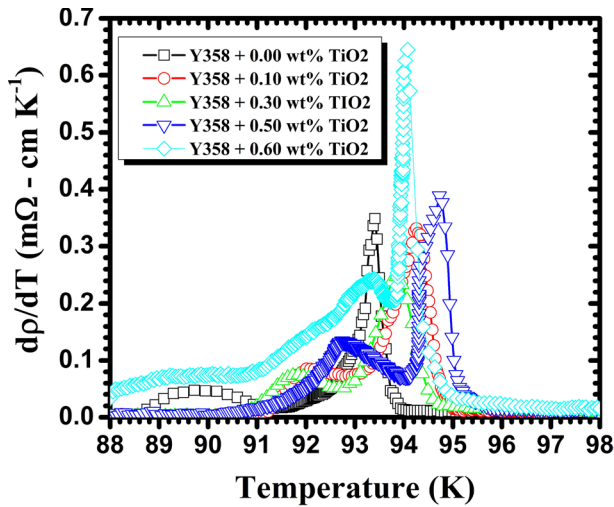


Fig. 7 Graphs of $d\rho/dT$ against T related to Y358 compounds with various amounts of nanoscale TiO_2 inclusions (color figure online)

to the $\Delta\sigma(T)$ intercept with the inverse of root temperature axis ($T^{-1/2}$). This procedure is shown in Fig. 8 for pure Y358 sample and related data for all of the specimen are recorded in Table 2. According to Fig. 8 at the low temperature up to the T_{LD} , the data are in good agreement with the 3D AL fluctuations. The mechanism of the fluctuation will be changed for the fluctuation pairs at the temperature T_{LD}^{HL} , based on the Hikami–Larkin (HL) model [59]. The T_C^p data obtained from both above mentioned

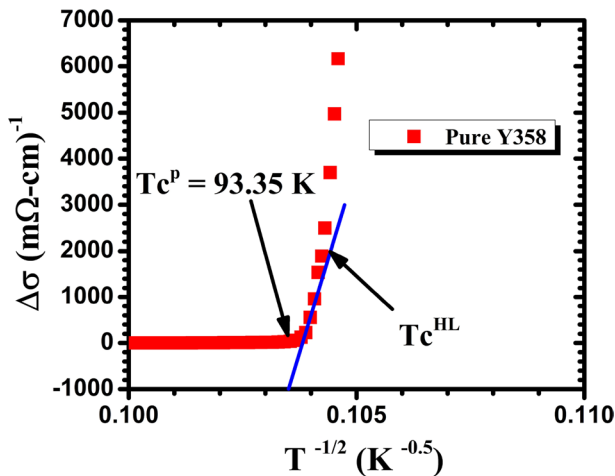


Fig. 8 Determination of T_C^p by $\Delta\sigma$ versus $T^{-1/2}$ curve. Linear extrapolated line from the point that $\Delta\sigma$ begins tending to zero, has the intercept on the inverse of root temperature axis. T_C^{HL} is anticipated via the Hikami–Larkin (HL) theory (color figure online)

criteria are almost identical and listed in Table 2 for all of the samples. By increasing TiO_2 nanoscale impurities, the T_C^P is improved for all of the doped samples. This improvement can be interpreted as intragrain variations due to the inclusion of titanium.

There is a wealth of literature on the nonlinear resistivity curve above T_c . This is the temperature regime where a lot of publications on the so-called pseudogap phase exist. There are even more theoretical papers on the origin of that pseudogap phase [60–62]. The resistivity curvature mapping (RCM) might be a tool for allowing one to obtain the pseudogap crossover line. Temperature dependence of the resistivity $\rho(T)$ around T_C^P related to the pure Y358 is shown in Fig. 9. This sample has been chosen because of the highest level of oxygen content compared to the TiO_2 added specimen. Determination of the exact hole doping p in the CuO_2 planes of YBCO is quite difficult, so oxygen content has been chosen instead [63]. Critical temperature of the samples is always sensitive to oxygen content [64]. According to Fig. 9, resistivity is linear from 92 to 93 K. Linear fit (green line) which obeys equation $\rho = \rho_0 + B T$ is also depicted. Here, $\rho_0 = -6.33 \pm 0.10$ and $B = 0.07 \pm 0.001$ are intercept and slope of the line, respectively. A simple power law $\rho(T) = \rho_0 + B T^n$, with the exponent $n = 1$ is the best match for resistivity. The exponent $n = 1$ reveals a non-Fermi-liquid behaviour [65], at temperature interval 92 - 93 K. This linear behaviour might be due to the pseudogap or the superconducting fluctuations (SCF), particularly when the SCF starts from completely a high temperature [66]. Also superconductivity reformed through the valence fluctuation was theoretically anticipated for the specific region of CeCu_2Si_2 [67]. From 93.5 to 94 K the resistivity polynomial fit (red curve) can be formulated as $\rho = \rho_0 + B_1 T + B_2 T^2$, where $\rho_0 = -1795.67 \pm 166.91$, $B_1 = 38.25 \pm 3.56$ and $B_2 = -0.20 \pm 0.019$. In this region, one can see the resistivity is not linear. Moreover, it can be shown that resistivity stays to be nonlinear versus temperature starts at 93.5 K in pseudogap phase. This property shows

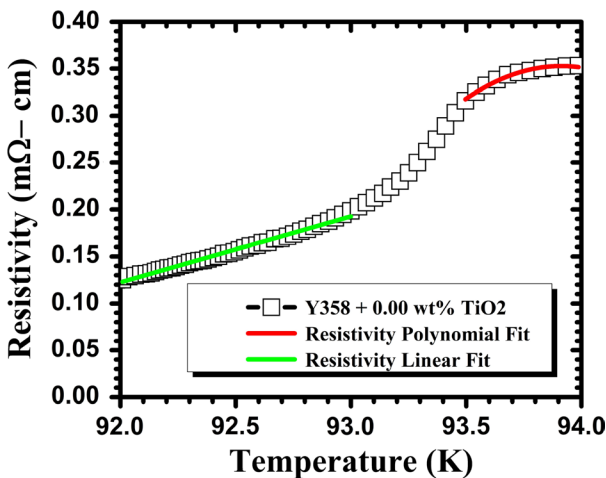


Fig. 9 Resistivity linear fit (green line) and polynomial fit (red curve) around T_C^P for pure Y358 sample, to investigate non-Fermi-liquid and Fermi-liquid behaviour (color figure online)

the Fermi-liquid behaviour in the resistivity of Y358 pristine sample at temperature higher than T_C^P . Thus, the two properties in different temperature regions around T_C^P are quite opposing: Fermi-liquid behaviour at temperature higher than critical temperature and non-Fermi liquid in the resistivity at interval temperature 92 - 93 K. Although temperature dependence of these different properties in the resistivity have been detected in another compounds [67, 68], but the source of these behaviour is still uncertain [69]. The resistivity of Y358 can equally be understood by classical SC theory such as AL and GL, while the nonlinear resistivity is taken as an indication of Fermi-liquid character. To elucidate the Fermi-liquid and non-Fermi-liquid behaviour much more studies, both theoretically and experimentally, should be done in various superconductors including pure and doped ones. The amount of $x=0.10$ to $x=0.60$ wt% TiO_2 addition, increases $T_{c \text{ onset}}$ compared to the pure sample. This happens because of the same spreading of nano-elements that cause the perfection of granule correlation. For polycrystalline superconductors, the $T_{c \text{ onset}}$ depends heavily on the intergranular development. The wide-ranging of superconductor transition which detected in the $\rho(T)$ is organised by clarification routes and depends profoundly upon the manufacture procedure. Diverse manufacture procedures such as annealing method are fundamental to specimen production. Increasing the annealed process interval might improve the critical temperature [70]. The Y358 synthesised by the melt-process might produce lower steady crystal arrangement than the solid-state feedback method [29]. However, assortment of fabrication can result in different critical parameters. This leads to the unlike imperfections, type of granule borders, granule concentrations and also dissimilarities in coupling influence among granules and by way of outcome dissimilar wider transition area.

For comparing the experimental data associated with excess conductivity ($\Delta\sigma$) to the theoretical model aimed at fluctuation conductivity, the plot of $\ln(\Delta\sigma)$ against $\ln(\epsilon)$ for pure and TiO_2 nanoscale added Y-358 specimens is illustrated in Fig. 10. To achieve this assessment, three remarkable fluctuation areas entitled critical, mid-field and short-wave fluctuation have chosen in each plot and are depicted in Fig. 10a–e. According to pure sample critical instability system related to $v_{cr} = 0.246 \pm 0.005$ is shown in Fig. 10a. For doped samples with TiO_2 nanoparticle values $x=0.10$ wt% to $x=0.60$ wt%, v_{cr} fit in the $(0.170 \pm 0.003 \leq v_{cr} < 0.226 \pm 0.006)$ area. This regime has been similarly identified in thin film [71], single crystal [72] and another polycrystalline [73] samples. Based on dynamical analytical scaling concept, it is predictable that $Z = 0.32$, whereas renormalisation collection computations anticipate $\Gamma = 0.67$ and $\eta = 0.03$ [74]. Verifying these quantities beside $D = 3$ estimates $v_{cr} = 0.33$. This can be respected by an original system established with the exponent $v_{cr} = 0.17$. This scaling behaviour which is named 3D-XY-E had been primary detected not only in yttrium [75–77] but also in bismuth-based high-temperature superconductors (HTSCs) [78]. According to Fig. 10, the critical fluctuation and three-dimensionality fluctuation areas interconnect at T_G . The dense lines in Gaussian areas characterise theoretic fits through the slopes of $-\frac{1}{2}$, -1 and $-\frac{3}{2}$ in the best interests of 3D, 2D and 1D regimes, respectively. The three discrete lined sections representing fluctuation conductivity behaviour in the mean-field region (M.F.R) start at T_G and end up at T_{1D-SW} . This area which is named Gaussian area is depicted in Fig. 10a at $(-3.6 \leq \ln(\epsilon) \leq -2.2)$ for pure sample. For other samples, this area

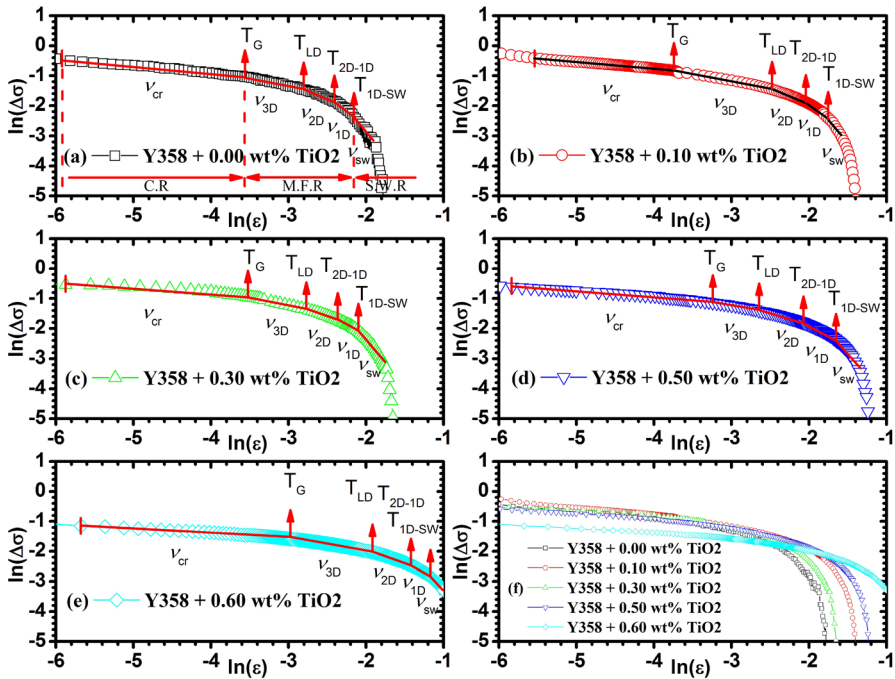


Fig. 10 Graph of $\ln(\Delta\sigma)$ against $\ln(\epsilon)$ of the Y358+x wt% TiO₂ nanoparticles doped ($x = 0.00, 0.10, 0.30, 0.50$ and 0.60) specimens. The dense streaks signify v_{cr} ($0.170 \pm 0.003 \leq v_{cr} \leq 0.246 \pm 0.005$ for critical region), the theoretical slopes $-0.5, -1, -1.5$ and -3 related to 3-D, 2-D, 1-D and S.W schemes, individually. The critical, mean-field and short-wave region are symbolised by C.R., M.F.R. and S.W.R. congruently (color figure online)

can be obtained at reduced temperature ($-3.8 < \ln(\epsilon) < -1.4$) related to Fig. 10b–e. To compare all graphs clearly they are grouped altogether in Fig. 10f. It should be pointed out that excess conductive region which is at or around the transition temperature is the main field of this study, even more since the T_c increases with TiO₂ insertion is not very big.

The intercepts of linear fit for the conductivity exponent values 0.5 differ from -2.665 ± 0.003 to -2.997 ± 0.001 , indicating the presence of three-dimensionality fluctuations. The zero-temperature coherence length alongside the c direction, $\xi_c(0)$ is calculated by determination of A_{3D} . These parameters ($\xi_c(0)$) vary from 10.93 Å to 15.24 Å, related to the Y358+x wt.% TiO₂ compounds, and are tabulated in Table 3. Among these data on behalf of a no added specimen when $x=0.00$, $\xi_c(0)$ is $\sim 0.2\%$ lower than the literature reported (10.95 Å) for Y358 pure sample. However, the smallest $\xi_c(0)$ in the sequence was 10.93 Å related to $x = 0.00$ and by rising nanoscale TiO₂ doping, $\xi_c(0)$ increased which shows less disarray stately of the composites [28].

The existence of 2D fluctuations can be confirmed once the conductivity proportion quantities approach to -1 . In this case, the intercepts of lined fitting differ around -4.24 ± 0.008 to -3.896 ± 0.002 . Afterwards, estimated amounts for

Table 3 Typical factors associated with extra conductivity instability study for Y358 mixtures with diverse quantities of TiO₂ nanoscale impurities. [F. M (First Method), S. M (Second Method), C. R (Critical Region), S.W (Short Wave)]

Parameters	x=0.00	x=0.10	x=0.30	x=0.50	x=0.60
Slopes of linear fit for C.R (v_{cr})	-0.246±0.005	-0.226±0.006	-0.187±0.016	-0.195±0.006	-0.170±0.003
Intercepts of linear fit related to v_{cr}	-1.894±0.023	-1.663±0.022	-1.56±0.067	-1.722±0.023	-2.072±0.009
Intercepts of linear fit when $v_{3D} = 0.5$	-2.665 ±0.003	-2.691±0.004	-2.717±0.004	-2.726±0.002	-2.997±0.001
Intercepts of linear fit when $v_{2D} = 1$	-4.24±0.008	-3.911±0.003	-4.097±0.005	-3.97±0.009	-3.896±0.002
Intercepts of linear fit when $v_{1D} = 1.5$	-5.499±0.008	-4.945±0.002	-5.235±0.004	-4.846±0.008	-4.582±0.002
Intercepts of linear fit when $v_{sw} = 3$	-8.837±0.019	-7.68±0.01	-8.375 ±0.011	-7.303±0.014	-6.343±0.004
Coherence Length $\xi_c(0)$ (Å)	10.93	11.21	11.51	11.62	15.24
Super-layer length F. M d (Å)	105.57	76.02	91.50	80.61	74.87
Super-layer length S. M d (Å)	88.47	77.52	84.18	87.38	80.24
Interlayer Coupling F. M J	0.043	0.087	0.063	0.083	0.166
Interlayer Coupling S. M J	0.061	0.084	0.075	0.071	0.144
Anisotropy γ	0.915	0.892	0.869	0.861	0.656

A_{2D} hints to obtain the super-layer distance d . Related to the Y358+x wt.% TiO₂ (x=0.00 to x=0.60) composites, the super-layer length d which are obtained by formula named First Method. These data vary from 105.57 Å to 74.87 Å and are listed in Table 3. The crossover temperatures 3D–2D which named T_{3D-2D} are computed by the junction of the two lined sections and subsequently by replacement of T_{3D-2D} accompanied with $\xi_c(0)$ to Equation 9, the super-layer distance d is attained and entitled Second Method. This issue (d) differs from 88.47 Å to 80.24 Å, on behalf of the x=0.00 to x=0.60 wt% TiO₂ samples, respectively. To compare the values associated with these two methods, a plot of the super-layer distance d vs. TiO₂ impurity is depicted accompanied with their mean value in Fig. 11. Once-over of this graph denotes that by rising nanoparticles titania doping the anisotropy γ and super-layer distance d decrease (refer to Table 3). The reduction of d indicates the diminishing of the mean free path aimed at the charge transporters upon the increase in TiO₂ doping. Decrease in anisotropy γ indicates that superconductivity is enhanced with addition of titania nanoparticles. The higher superconducting phase compounds possess low-grade anisotropy factors than the lesser superconducting phase composites. The anisotropy factor is proportional to the non-superconducting phase, so the further normal phase creates

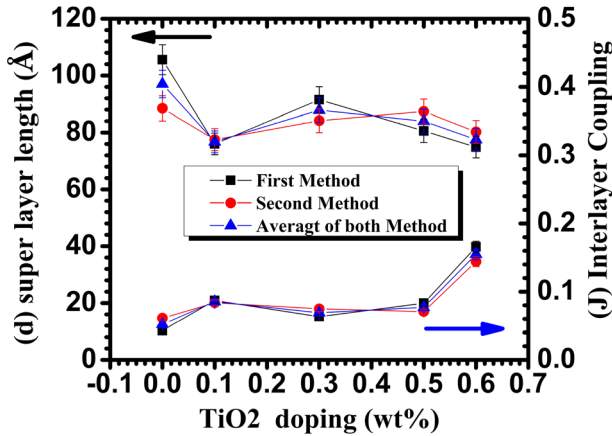


Fig. 11 The superconducting parameters d and J against diverse doping related to the $Y358+x$ wt.% TiO_2 mixtures with twofold processes and their middling (color figure online)

extra anisotropy [79]. Although cuprate superconductors display strong anisotropy which depends on coherence length (ξ) and direction, main factor is width of vortex core identical to coherence length (ξ). Above this width, the electrons creating Cooper pairs though are able to influence one to another [80].

According to AL and LD context, the interlayer coupling J increase in general and their averages change from 0.052 to 0.155 by increasing of TiO_2 nanoparticles from $x=0.00$ to $x=0.60$ wt.%, respectively. This increase in J specifies the dependency on dislocation of each atom because of the rise in TiO_2 impurity (inspect Table 3 and Fig. 11).

Diverse temperatures connected with their dimensionality instability and correlated to numerous TiO_2 nanoparticles substance are listed in Table 4. Exhibiting this chart, T_c lesser than T_{LD} , designates that the thermodynamically triggered Cooper pairs are created inside the granule at relatively higher temperatures. Nevertheless, because of the intragranular instabilities the Gaussian critical temperature declines to an inferior rate. It is likely to conclude that the 3D Gaussian system, controls the three-dimensional boundary for obtaining the distant information related to the bulk

Table 4 TiO_2 nanoscale substance dependency of diverse intersect temperatures (GL, LD and SWF) complement with their temperature variety

Parameters	$x=0.00$	$x=0.10$	$x=0.30$	$x=0.50$	$x=0.60$
$T_G(K)$	96.05	96.50	97.81	98.44	98.86
$T_{LD}(K)$	99.11	102.16	100.85	101.45	107.63
$T_{2D-1D}(K)$	101.76	106.70	103.95	106.80	116.94
$T_{1D-SWF}(K)$	104.22	110.37	106.45	112.71	123.21
$\Delta T_{v_{1D}}(K)$	2.46	3.67	2.50	5.91	6.27
$\Delta T_{v_{2D}}(K)$	2.65	4.54	3.10	5.35	9.31
$\Delta T_{v_{3D}}(K)$	3.06	5.66	3.04	3.01	8.77

Table 5 Computed critical issues related to none added and doped Y358 specimens by different quantities of nanoscale TiO₂ insertions

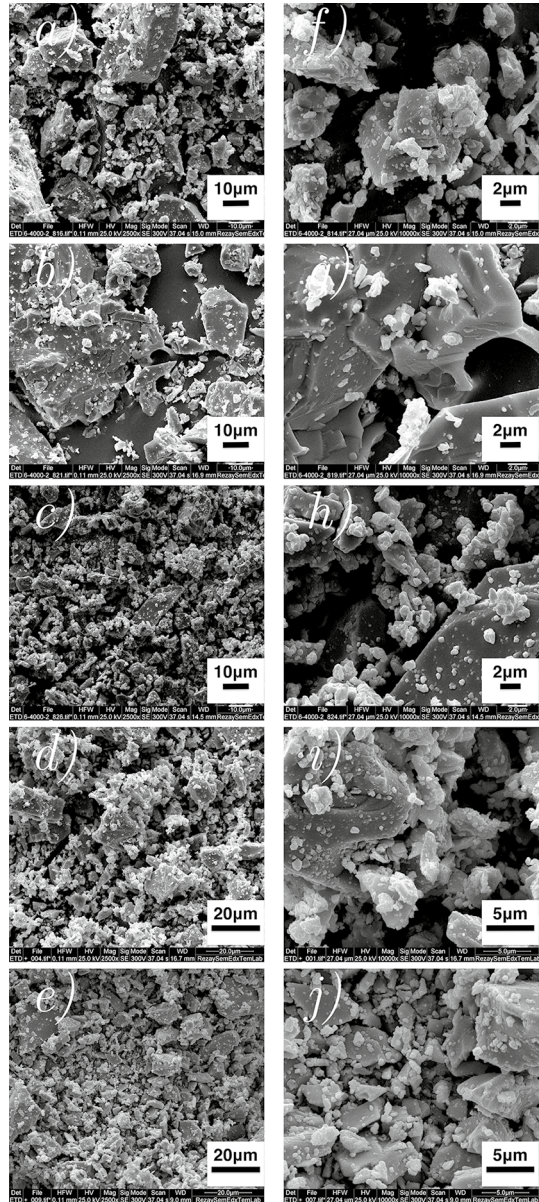
Parameters	x=0.00	x=0.10	x=0.30	x=0.50	x=0.60
$B_c(0)(T)$	21.29	20.75	20.22	20.03	15.27
$B_{c1}(0)(T)$	3.64	3.60	3.56	3.54	3.09
$B_{c2}(0)(T)$	275.52	261.66	248.49	243.72	141.76
$J_c(0)A/m^2 \times 10^9$	1.16	1.13	1.10	1.09	0.83
$J_c(0)A/cm^2$	115901.48	112948.33	110069.33	109007.91	83137.05

superconductors [81]. While the temperature is reduced nearby T_c , primary superconductivity would be generated in the CuO₂ surfaces, by way of a two-dimensionality system, and then intersects to a distinct three-dimensionality system [82].

Figure 12 demonstrates the scanning electron microscopy (SEM) pictures with magnification 2500 (a, b, c, d and e) and 10000 (f, g, h, i and j) related to the non-added $Y_3Ba_5Cu_8O_{18\pm\delta}$ superconducting sample and doped by various ($x=0.00$, $x=0.10$, $x=0.30$, $x=0.50$ and $x=0.60$) nanoscale TiO₂ additions specimens. This image exhibits that the arbitrary alignment of granules and nanoscale titanium-oxide additions affect reduction of the particle dimension in Y358 samples associated with $x=0.00$, $x=0.10$ and $x=0.30$ wt% which confirms by the average crystallite size value 35.47, 29.76 and 32.55 (nm), respectively. In the cases of $x=0.50$ and $x=0.60$ wt%, the average crystallite size value increases to 41.47 and 42.11 (nm) correspondingly. In these two series of pictures, one might be able to detect that, with cumulating the nanoscale TiO₂ doping up to $x=0.30$ wt% the uniformity of the specimens and also junction among the particles is enhanced. Inferior dimensional influences in the transportation parameters would be appeared by the shrinkage in particle volume while the sum of granule borders upsurges and subsequently implies a larger quantity of feeble contacts (inspect Ref. [83]). Consideration of the microstructure specimen validates clearly that insertion of TiO₂ nanoparticles recover the grain connectivity and decreases the fractures and cavities among the granules and subsequently increases the grain size. In this scenario, each grain influence and drive others and arrange a boundary where the atomic alignment varies with various amounts of TiO₂ inclusions. This effect does not give monotonous change and might be a reason for none monotonous superconducting properties of the compounds.

The scanning electron micrographs of $Y_3Ba_5Cu_8O_{(18\pm\delta)}$ sample with 0.50 wt% TiO₂ nanoparticles doped with magnification 2500× are illustrated in Fig. 13. The SEM image with $x=0.50$ wt% TiO₂ doped is chosen because of the high value of average crystallite size compared to the non-added sample. In this figure, “Normal” and “Modified” SEM images are labelled A and B, respectively, which is corresponding to Fig. 12d. To compare these two images for better exhibition of particles, the pixels intensity below the minimum threshold value is displayed in blue (background contribution) and the pixels intensity above the maximum threshold value is depicted in green colour. However, it is obvious that Fig. 13a, b displays an augmentation of granule volume and trimness configurations by way of the TiO₂

Fig. 12 Scanning electron micrographs of $Y_3Ba_5Cu_8O_{(18\pm\delta)}$ compounds plus 0.0 (a, f), 0.10 (b, g), 0.30 (c, h), 0.50 (d, i) and 0.60 wt.% (e, j) (magnification 2500 and 10000 correspondingly) TiO_2 nanoscale doping. The arbitrary alignment of particles and nearly reformation of granules connection in specific parts is obvious. [Each bar = $10\mu m$ in the images (a), (b), (c) $20\mu m$ in the images (d), (e)] and [$2\mu m$ in the images (f), (g), (h) $5\mu m$ in the images (i), (j)] upon magnification [2500] and [10000], respectively



supplement increases in this specific amount ($x = 0.50$). The particles similarly look to lengthen further at one lateral, establishing an almost oblong-similar arrangement with a regular measure of $1.75\ \mu m$. This estimation comes up by comparison of the grains length with the bar length ($20\ \mu m$) which is shown in the image.

From Equations 15 to 18, the critical parameters such as critical magnetic fields and current density, $B_c(0)$, $B_{c1}(0)$, $B_{c2}(0)$ and $J_c(0)$ aimed at none added and impure

compounds are calculated and tabulated in Table 5. Obtaining all of superconducting parameters shows that the theory outlined in the chapter “Excess conductivity model” is sufficient to describe our results. Comparing entirely the quantities of $B_c(0)$, $B_{c1}(0)$, $B_{c2}(0)$, and critical current density $J_c(0)$ on behalf of pure with the impure Y358 compounds, displays by rising the nano-sized titania insertions, the mentioned critical parameters are decreased. This scenario can be interpreted equally “the valence state of Ti^{4+} is larger than that of Cu^{2+} , and substitution of Ti for Cu might decline the moveable carrier concentration because of hole filling by Ti ” [23] which indicates the destruction of flux pinning properties.

5 Conclusion

High-temperature superconductors Y-358 polycrystalline have been synthesised by the conventional solid-state reaction route with titanium dioxide (TiO_2) anatase nanoparticles addition at $x = 0.0$ to 0.60 wt.%. The (XRD) and (SEM) techniques implemented to inspect phase formation and microstructures methodically. The Rietveld refinement technique concerning XRD revealed that by rising the amount of nano-size TiO_2 in Y58 substance the crystal lattice constants altered slightly and the orthorhombicity overall reduced. The crystallite size calculation and SEM observations show that compared to the titania-free sample the grain size and the average crystallite size decreased with increasing the amount of TiO_2 up to $x=0.30$ in the yttrium-based superconductor Y-358 specimens. The resistivity-temperature graphs exhibited metallic and superconducting conduct throughout the records, respectively, with and without the TiO_2 nanoparticles doping. The AL and LD outline was used to investigate the effect of titania nanoparticles on the conductivity fluctuation of our samples. Nanoparticles TiO_2 insertion as dope entities to the Y-358 matrix proves the effect in enhancing some superconductor properties, in specific, T_c in every specimens. In brief, the theory outlined in the chapter “Excess conductivity model” is sufficient to describe our results.

Structural and dimensional modifications associated with the electrical transport properties by addition of TiO_2 nano-size inclusion can be stated as allocation of TiO_2 distributed to the Y-358 structure and resultant different levels of irregularities

in the composite. These outcomes might be ascribed as the presence of disorder due to a quantity of replaced copper positions in Y358. This phenomenon effects in an electrical configuration change of the granules, and therefore, the lack of an optimised carrier concentration in the CuO₂ planes. Results display that with increasing TiO₂ dope, Cu (1) sites occupy by Ti and cause the reduction in orthorhombicity. In the YBCO polycrystalline system, an increase in nanoparticles TiO₂ insertions, causes an enhanced status of disarray and influences the superconducting and pinning properties. By increasing TiO₂ inclusion, T_c and the overall interlayer coupling J increase but anisotropy γ and super-layer distance d decrease. These results might be related to the redistribution of charges in the superconducting scheme associated with oxygen substance, displacement per atom, the number of substitution sites and opponent of the weak bond produced through irregularities, respectively. T_{LD} increased in the compounds with TiO₂ doping which designates the dominant type of instability of cooper pairs in three-dimensionality region. Variation of lattice constants, average crystal size, crystallite dimensions and calculated density display the penetration of titania into the superconducting grains. GL equations and number were used to compute some critical parameters as $B_{c1}(0)$, $B_{c2}(0)$ and $J_c(0)$ indirectly. These parameters were lower when the titania nanoparticles were introduced to the compounds compared to the pure one which indicate inferior flux pinning in TiO₂ added samples.

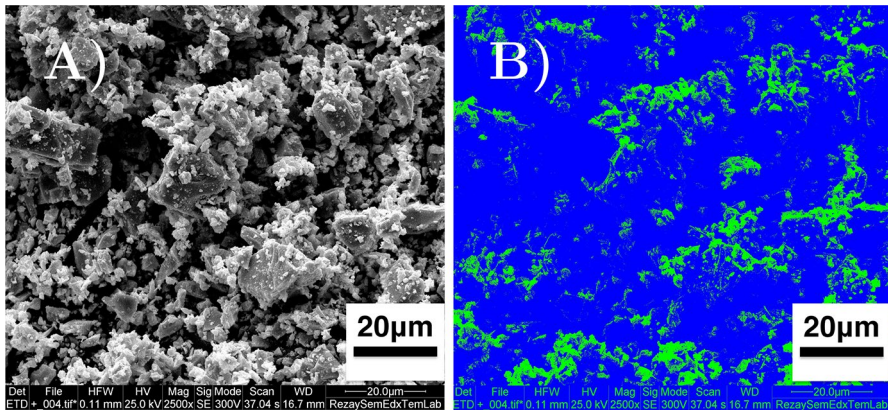


Fig. 13 Scanning electron micrographs of $Y_3Ba_5Cu_8O_{(18\pm\delta)}$ mixtures by 0.50 wt.% TiO₂ nanoparticles doped with magnification 2500 \times . A) Normal SEM image, B) modified SEM image, the pixels intensity below the minimum threshold value displayed in blue (background contribution) and the pixels intensity above the maximum threshold value depicted in green colour for better exhibition of particles (color figure online)

Acknowledgements The authors would like to thank Mr. Fatemi, for his assistance through the preparation of the samples. Special thanks go to Mr. Jamali and Mr. Nowroozi from Islamic Azad University-Shiraz Branch and Mr. Mahmoodinezhad from the Brandenburg University of Technology, Germany, for their support and suitable notions.

Declarations

Conflict of interest The authors declare that they have no conflict of interest.

References

1. J.G. Bednorz, K.A. Müller, *Zeitschrift für Physik B Condens Matter* **64**(2), 189 (1986). <https://doi.org/10.1007/BF01303701>
2. P. Freitas, C. Tsuei, T. Plaskett, *Phys. Rev. B* **36**(1), 833 (1987). <https://doi.org/10.1103/PhysRevB.36.833>
3. M. Ausloos, C. Laurent, *Phys. Rev. B* **37**(1), 611 (1988). <https://doi.org/10.1103/PhysRevB.37.611>
4. F. Vidal, J. Veira, J. Maza, F. Miguelez, E. Moran, M. Alario, *Solid State Commun.* **66**(4), 421 (1988). [https://doi.org/10.1016/0038-1098\(88\)90869-1](https://doi.org/10.1016/0038-1098(88)90869-1)
5. F. Vidal, J. Veira, J. Maza, F. Garcia-Alvarado, E. Moran, M. Alario, *J. Phys. C: Solid State Phys.* **21**(16), L599 (1988). <https://doi.org/10.1088/0022-3719/21/16/009>
6. W. Skocpol, M. Tinkham, *Rep. Prog. Phys.* **38**(9), 1049 (1975). <https://doi.org/10.1088/0034-4885/38/9/001>
7. E. Rostamabadi, S.R. Ghorbani, X. Wang, *Euro. Phys. J. B* **92**(5), 94 (2019). <https://doi.org/10.1140/epjb/e2019-100063-8>
8. E. Talantsev, N. Strickland, P. Hoefakker, J. Xia, N. Long, *Curr. Appl. Phys.* **8**(3–4), 388 (2008). <https://doi.org/10.1016/j.cap.2007.10.036>
9. E. Giannini, R. Gladyshevskii, N. Clayton, N. Musolino, V. Garnier, A. Piriou, R. Flükiger, *Curr. Appl. Phys.* **8**(2), 115 (2008). <https://doi.org/10.1016/j.cap.2007.04.014>
10. J. Gosner, B. Kubala, J. Ankerhold, *Phys. Rev. B.* (2019). <https://doi.org/10.1103/PhysRevB.99.144524>
11. V.N. Vieira, P. Pureur, J. Schaf, *Phys. Rev. B.* (2002). <https://doi.org/10.1103/PhysRevB.66.224506>
12. I. Bouchoucha, F. Ben Azzouz, M. Ben Salem, *J. Supercond. Nov. Magn.* (2011). <https://doi.org/10.1007/s10948-010-1007-2>
13. B. Sahoo, K.L. Routray, B. Panda, D. Samal, D. Behera, *J. Phys. Chem. Solids* **132**(April), 187 (2019). <https://doi.org/10.1016/j.jpcs.2019.04.035>
14. S.N. Abd-Ghani, H.K. Wye, K. Ing, R. Abd-Shukor, K. Wei, *Adv. Mater. Res.* (2014). <https://doi.org/10.4028/www.scientific.net/AMR.895.105>
15. X. Cui, G. Liu, J. Wang, Z. Huang, Y. Zhao, B. Tao, Y. Li, *Physica C: Superconduct.* **466**(1–2), 1 (2007). <https://doi.org/10.1016/j.physc.2007.04.223>
16. C. Wang, J. Li, J. Dho, *Mater. Sci. Eng.: B* **182**, 1 (2014). <https://doi.org/10.1016/j.mseb.2013.11.021>
17. S.X. Zhang, D.C. Kundaliya, W. Yu, S. Dhar, S.Y. Young, L.G. Salamanca-Riba, S.B. Ogale, R.D. Vispute, T. Venkatesan, *J. Appl. Phys.* (2007). <https://doi.org/10.1063/1.2750407>
18. T. Nakamura, T. Ichitsubo, E. Matsubara, A. Muramatsu, N. Sato, H. Takahashi, *Acta Materialia* **53**(2), 323 (2005). <https://doi.org/10.1016/j.actamat.2004.09.026>
19. T. Luttrell, S. Halpegamage, J. Tao, A. Kramer, E. Sutter, M. Batzill, *Sci. Rep.* **4**, 1 (2015). <https://doi.org/10.1038/srep04043>
20. N.A. Hamid, R. Abd-Shukor, *J. Mater. Sci.* **35**(9), 2325 (2000). <https://doi.org/10.1023/A:1004759801684>
21. G.J. Xu, J.C. Grivel, A. Abrahamsen, N. Andersen, *Physica C: Superconduct.* **406**(1–2), 95 (2004). <https://doi.org/10.1016/j.physc.2004.03.235>
22. P. Rejith, S. Vidya, J. Thomas, *Materials Today: Proceedings* **2**(3), 997 (2015). <https://doi.org/10.1016/j.matpr.2015.06.024>
23. M. Sahoo, D. Behera, *J Superconduct Novel Magn* **27**(1), 83 (2014). <https://doi.org/10.1007/s10948-013-2269-2>
24. G. Shams, A. Mahmoodinezhad, M. Ranjbar, *Iran J. Sci. Technol Trans. A Sci.* **42**(4), 2337 (2018). <https://doi.org/10.1007/s40995-017-0451-2>

25. N.A. Khalid, M.M.A. Kechik, N.A. Baharuddin, C.S. Kien, H. Baqiah, N.N.M. Yusuf, A.H. Shaari, A. Hashim, Z.A. Talib, *Ceram. Int.* **44**(8), 9568 (2018). <https://doi.org/10.1016/j.ceramint.2018.02.178>
26. Y. Slimani, E. Hannachi, A. Ekicibil, M. Almessiere, F.B. Azzouz, *J. Alloys Compd.* **781**, 664 (2019). <https://doi.org/10.1016/j.jallcom.2018.12.062>
27. A. Aliabadi, Y. Akhavan Farshchi, M. Akhavan, *Phys. C Supercond. Appl.* (2012). <https://doi.org/10.1016/j.physc.2009.09.003>
28. Y. Slimani, E. Hannachi, M.B. Salem, A. Hamrita, M.B. Salem, F.B. Azzouz, *J. Superconduct. Novel Magn.* **28**(10), 3001 (2015). <https://doi.org/10.1007/s10948-015-3144-0>
29. S. Sangchaisri, N. Longhan, T. Kruaehong, *J. Mater. Sci. Appl. Energy* **6**(3), 233 (2017)
30. G. Shams, M. Ranjbar, *Braz. J. Phys.* (2019). <https://doi.org/10.1007/s13538-019-00701-5>
31. A. Cohen, B. Matei, *Tutorials on Multiresolution in Geometric Modelling* (Springer, Berlin, 2002)
32. L. Aslamazov, A. Larkin, 30 Years of the Landau Institute-Selected Papers. *World Sci* (1996). https://doi.org/10.1142/9789814317344_0004
33. P. Pureur, R.M. Costa, P. Rodrigues Jr., J. Kunzler, J. Schaf, L. Ghivelder, J. Campá, I. Rasines, *Physica C: Superconduct.* **235**, 1939 (1994). [https://doi.org/10.1016/0921-4534\(94\)92191-1](https://doi.org/10.1016/0921-4534(94)92191-1)
34. A. Esmaeili, H. Sedghi, M. Amniat-Talab, M. Talebian, *Eur. Phys. J. B* **79**(4), 443 (2011). <https://doi.org/10.1140/epjb/e2011-10814-x>
35. Y. Zhao, C.H. Cheng, J.S. Wang, *Supercond. Sci. Technol* **18**(2), S43 (2005). <https://doi.org/10.1088/0953-2048/18/2/010>
36. S.W. Tozer, A.W. Kleinsasser, T. Penney, D. Kaiser, F. Holtzberg, *Phys. Rev. Lett.* **59**(15), 1768 (1987). <https://doi.org/10.1103/PhysRevLett.59.1768>
37. T.R. Dinger, T.K. Worthington, W.J. Gallagher, R.L. Sandstrom, *Phys. Rev. Lett.* **58**(25), 2687 (1987). <https://doi.org/10.1103/PhysRevLett.58.2687>
38. X. Tang, Q. Liu, J. Wang, H. Chan, *Appl. Phys. A* **96**(4), 945 (2009). <https://doi.org/10.1007/s00339-009-5103-8>
39. A.A. Yusuf, A. Yahya, N.A. Khan, F.M. Salleh, E. Marsom, N. Huda, *Physica C: Superconduct.* **471**(11–12), 363 (2011). <https://doi.org/10.1016/j.physc.2011.03.007>
40. M. Cimberle, C. Ferdeghini, E. Giannini, D. Marre, M. Putti, A. Siri, F. Federici, A. Varlamov, *Phys. Rev. B* **55**(22), R14745 (1997). <https://doi.org/10.1103/PhysRevB.55.R14745>
41. N.A. Khan, N. Hassan, M. Irfan, T. Firdous, *Physica B: Condens. Matter* **405**(6), 1541 (2010). <https://doi.org/10.1016/j.physb.2009.12.036>
42. M. Farbod, M.R. Batvandi, *Physica C: Superconduct.* **471**(3–4), 112 (2011). <https://doi.org/10.1016/j.physc.2010.11.005>
43. U. Holzwarth, N. Gibson, *Nat. Nanotechnol.* **6**(9), 534 (2011). <https://doi.org/10.1038/nnano.2011.145>
44. A. Tavana, M. Akhavan, *Eur. Phys. J. B* **73**(1), 79 (2010). <https://doi.org/10.1140/epjb/e2009-00396-7>
45. A.O. Ayaş, A. Ekicibil, S.K. Çetin, A. Coşkun, A.O. Er, Y. Ufuktepe, T. Firat, K. Kıymaç, *J. Supercond. Nov. Magn.* **24**(8), 2243 (2011). <https://doi.org/10.1007/s10948-011-1192-7>
46. Y. Slimani, E. Hannachi, M. Ben Salem, A. Hamrita, A. Varilci, W. Dachraoui, M. Ben Salem, F. Ben Azzouz (2014) *Phys Matter B Condens. Doi*: <https://doi.org/10.1016/J.PHYSB.2014.06.003>
47. A. Kulpa, A. Chaklader, N. Osborne, G. Roemer, B. Sullivan, D. Williams, *Solid State Commun.* **71**(4), 265 (1989). [https://doi.org/10.1016/0038-1098\(89\)91011-9](https://doi.org/10.1016/0038-1098(89)91011-9)
48. Y. Xu, M. Suenaga, J. Taftø, R. Sabatini, A. Moodenbaugh, P. Zolliker, *Phys. Rev. B* **39**(10), 6667 (1989). <https://doi.org/10.1103/PhysRevB.39.6667>
49. L. Liu, C. Dong, J. Zhang, J. Li, *Phys. C Supercond* **377**(3), 348 (2002). [https://doi.org/10.1016/S0921-4534\(01\)01286-2](https://doi.org/10.1016/S0921-4534(01)01286-2)
50. A. Ramli, A.H. Shaari, H. Baqiah, C.S. Kean, M.M.A. Kechik, Z.A. Talib, *J. Rare Earths* **34**(9), 895 (2016). [https://doi.org/10.1016/S1002-0721\(16\)60112-6](https://doi.org/10.1016/S1002-0721(16)60112-6)
51. A. Öztürk, İ Düzgün, S. Çelebi, *J. Alloys Compd.* **495**(1), 104 (2010). <https://doi.org/10.1016/j.jallcom.2010.01.095>
52. M. Ben Salem, M. Almessiere, A. Al-Otaibi, M. Ben Salem, F. Ben Azzouz, *J. Alloys Compd.* **657**, 286 (2016). <https://doi.org/10.1016/j.jallcom.2015.10.077>
53. P. Benzi, E. Bottizzo, N. Rizzi, *J. Cryst. Growth* **269**(2–4), 625 (2004)
54. B.A. Albiss, N. Al-Rawashdeh, A. Abu Jabal, M. Gharaibeh, I.M. Obaidat, M.K. Hasan, K.A. Azez, *J. Supercond. Nov. Magn* **23**(7), 1333 (2010). <https://doi.org/10.1007/s10948-010-0777-x>

55. P. Udomsamuthirun, T. Kruaehong, T. Nilkamjon, S. Ratreng, J. Supercond. Nov. Magn. **23**(7), 1377 (2010). <https://doi.org/10.1007/s10948-010-0786-9>
56. H. Salamati, P. Kameli, Solid State Commun. **125**(7–8), 407 (2003)
57. A. Nur-Syazwani, R. Abd-Shukor, J. Superconduct. Novel Magn. **32**(4), 863 (2019)
58. A.A. Aly, N. Mohammed, R. Awad, H. Motaweh, D.E.S. Bakeer, J. Superconduct. Novel Magn. **25**(7), 2281 (2012). <https://doi.org/10.1007/s10948-012-1621-2>
59. S. Hikami, A. Larkin, Modern Phys. Lett. B **2**(05), 693 (1988)
60. Y. Ando, S. Komiya, K. Segawa, S. Ono, Y. Kurita, Phys. Rev. Lett. **93**(26), 267001 (2004)
61. T. Timusk, B. Statt, Rep. Prog. Phys. **62**(1), 61 (1999)
62. J. Orenstein, A. Millis, Science **288**(5465), 468 (2000)
63. K. Segawa, Y. Ando, Phys. Rev. B **69**(10), 104521 (2004)
64. R.A. Klemm, *Layer Superconduct.*, vol. 153 (Oxford University Press, England, 2012)
65. F. Kneidinger, H. Michor, E. Bauer, A. Griбанov, A. Lipatov, Y. Seropegin, J. Sereni, P. Rogl, Phys. Rev. B **88**(2), 024423 (2013)
66. Y. Ando, K. Segawa, Phys. Rev. Lett. **88**(16), 167005 (2002)
67. A.T. Holmes, D. Jaccard, K. Miyake, Phys. Rev. B **69**(2), 024508 (2004)
68. H. Yuan, F. Grosche, M. Deppe, G. Sparn, C. Geibel, F. Steglich, Phys. Rev. Lett. **96**(4), 047008 (2006)
69. N. Tsujii, H. Kitazawa, T. Aoyagi, T. Kimura, G. Kido, J. Magn. Mater. **310**(2), 349 (2007)
70. X. Chaud, T. Prikhna, Y. Savchuk, A. Joulain, E. Haanappel, P. Diko, L. Porcar, M. Soliman, Mater. Sci. Eng.: B **151**(1), 53 (2008). <https://doi.org/10.1016/j.mseb.2008.02.006>
71. P. Mayorga, D. Téllez, Q. Madueno, J. Alfonso, J. Roa-Rojas, Braz. J. Phys. **36**(3B), 1084 (2006). <https://doi.org/10.1590/S0103-97332006000600076>
72. J.R. Rojas, A. Jurelo, R.M. Costa, L.M. Ferreira, P. Pureur, M. Orlando, P. Prieto, G. Nieva, Physica C: Superconduct. **341**, 1911 (2000). [https://doi.org/10.1016/S0921-4534\(00\)01360-5](https://doi.org/10.1016/S0921-4534(00)01360-5)
73. M. Sahoo, D. Behera, J. Mater. Sci. Eng. **01**, 04 (2012). <https://doi.org/10.4172/2169-0022.1000115>
74. J.C. Le Guillou, J. Zinn-Justin, Phys. Rev. B **21**(9), 3976 (1980). <https://doi.org/10.1103/PhysRevB.21.3976>
75. W. Holm, Y. Eltsev, Ö. Rapp, Phys. Rev. B **51**(17), 11992 (1995). <https://doi.org/10.1103/PhysRevB.51.11992>
76. J.T. Kim, N. Goldenfeld, J. Giapintzakis, D.M. Ginsberg, Phys. Rev. B **56**(1), 118 (1997). <https://doi.org/10.1103/PhysRevB.56.118>
77. A.R. Jurelo, J.V. Kunzler, J. Schaf, P. Pureur, J. Rosenblatt, Phys. Rev. B **56**(22), 14815 (1997). <https://doi.org/10.1103/PhysRevB.56.14815>
78. R. Menegotto Costa, P. Pureur, L. Ghivelder, J.A. Campá, I. Rasines, Phys. Rev. B **56**(17), 10836 (1997). <https://doi.org/10.1103/PhysRevB.56.10836>
79. S. Sujinnapram, P. Udomsamuthirun, T. Kruaehong, T. Nilkamjon, S. Ratreng, Bullet. Mater. Sci. **34**(5), 1053 (2011). <https://doi.org/10.1007/s12034-011-0130-4>
80. V. Bartúněk, O. Smrčková, Ceram. - Silikaty **54**(2), 133 (2010). http://www.ceramics-silikaty.cz/index.php?page=cs_detail_doi&id=351
81. J. Roa-Rojas, D.L. Téllez, M. Rojas Sarmiento, Braz. J. Phys. (2006). <https://doi.org/10.1590/s0103-97332006000600081>
82. A. Kujur, D. Behera, Thin Solid Films **520**(6), 2195 (2012). <https://doi.org/10.1016/j.tsf.2011.11.008>
83. X. Wang, J. Horvat, G. Gu, K. Uprety, H. Liu, S. Dou, Physica C: Superconduct. **337**(1–4), 221 (2000). [https://doi.org/10.1016/S0921-4534\(00\)00105-2](https://doi.org/10.1016/S0921-4534(00)00105-2)